THE JOURNAL OF PHYSICAL CHEMISTRY C
A JOURNAL OF THE AMERICAN CHEMICAL SOCIETY

pubs.acs.org/JPCC

Article

MgPdSb—An Electron-Deficient Half-Heusler Phase

Michał J. Winiarski, Kamila Stolecka, Leszek Litzbarski, Thao T. Tran, Karolina Górnicka, and Tomasz Klimczuk*

Cite This: *J. Phys. Chem. C* 2022, 126, 14229–14235

Read Online

ACCESS | Metrics & More | Article Recommendations | Supporting Information

ABSTRACT: The half-Heusler family consists of many semiconducting intermetallic compounds, virtually all of them having a valence electron count (VEC) of 18. We have studied an electron-deficient (VEC = 17) phase MgPdSb and its Pd-stuffed variant $MgPd_{1.25}Sb$. The cubic $F\bar{4}3m$ crystal structure was confirmed by the Rietveld refinement of powder X-ray diffraction (XRD) data. The lattice parameter is a = 6.284 and 6.335 Å for MgPdSb and $MgPd_{1.25}Sb$, respectively. The Debye temperature and Sommerfeld coefficient for MgPdSb are Θ_D = 282 K and γ = 3.3 mJ mol^{-1} K^{-2}, respectively, and are similar to those obtained for $MgPd_{1.25}Sb$. There is neither phase transition nor superconductivity observed above 1.8 K. The differences between the electronic structures of Mg-based half-Heusler compounds make them robustly metallic, irrespective of the electron count and the introduction of interstitial transition metal (Pd) atoms.

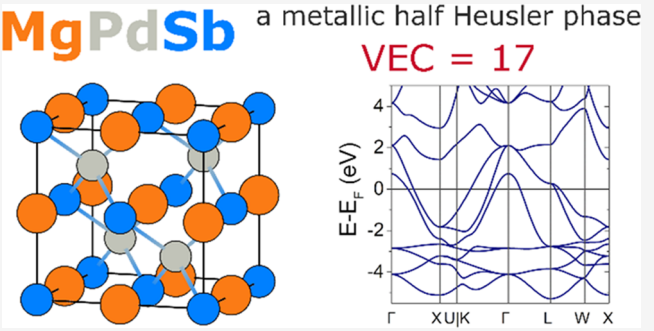

INTRODUCTION

The large and diverse family of Heusler compounds attracts an unwavering research interest due to the versatility and tunability of their physical properties. The Heusler structure ($MnCu_2Al$ type) can be viewed as a simple NaCl-type network with all of the octahedral voids occupied (see Figure 1a). In the so-called half-Heusler structure only every other void is filled, resulting in a noncentrosymmetric network (Figure 1b), an ordered ternary variant of the zinc blende (ZnS) structure.[1,2]

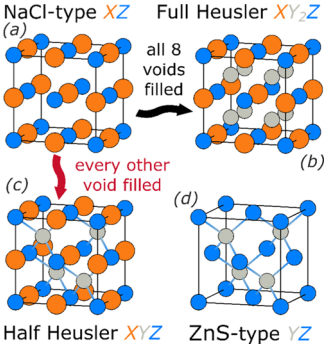

Figure 1. Relationships between NaCl (a), full-Heusler (b), half-Heusler (c), and zinc blende (ZnS) (d) structure types. Heusler phases are NaCl-type structures with either all (full-Heusler) or every other octahedral void (half-Heusler) filled by a third atom type. Half-Heusler cell can also be viewed as a ternary analogue of a zinc blende structure.

Interesting properties are often found in half-Heusler compounds, including a relatively high thermoelectric performance,[3−6] topologically nontrivial electronic states,[7−10] and superconductivity.[9,11,12]

The half-Heusler is the 15th most common structure type among reported intermetallics.[13] Most of half-Heusler phases have a valence electron count (VEC) of 8, 18, or 28 (per formula unit), corresponding to a closed-shell configuration and, very often, semiconducting properties.[3,14−17] The Materials Project database lists 135 unique half-Heusler phases (see the Supporting Material Table S1 and Figure S1 for more details): 102 of these compounds have VEC = 8, 18, or 28 and only 15% (21 compounds) are electron-deficient with VEC = 16 or 17. It is often observed that phases with VEC deviating from 8, 18, or 28 are stabilized by either interstitial defects (for electron-deficient compounds, such as $TiFe_{1+x}Sb$) or vacancies (electron-rich compounds, e.g., $Ti_{1-x}NiSb$).[15,17]

The general formula for a half-Heusler compound can be represented as *XYZ*. For VEC = 18 and 28, an electropositive element (early transition metal, rare earth metal, Li, or Mg) occupies the *X* position, *Y* is a late transition metal, and *Z* is a *p*-block metal. Only 16 out of the 135 phases included in the

Received: February 25, 2022
Revised: August 1, 2022
Published: August 15, 2022

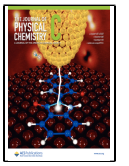

Materials Project database have a main group element (Li or Mg) at the *X* position.

In this article, we describe the synthesis and characterization of a stable electron-deficient MgPdSb (VEC = 17) half-Heusler compound, which was first reported by Drews *et al.*[18] We discuss its physical properties based on chemical bonding considerations. No significant concentration of interstitial defects is observed in the parent compound, yet a surplus Pd can be introduced into the structure. The presence of Mg at the *X* site results in a qualitatively different electronic structure, compared to transition metal-bearing half-Heusler compounds.

MATERIALS AND METHODS

A polycrystalline sample of MgPdSb was prepared by a solid-state reaction of Mg and PdSb, as described in the Supporting Material, with a 5% Mg surplus to account for its evaporation loss. The same method was recently used for the synthesis of a full-Heusler phase $MgPd_2Sb$.[19] In addition to the stoichiometric MgPdSb, a series of $MgPd_{1+x}Sb$ (x = 0.25, 0.50, 0.75) was synthesized, in which the additional Pd atoms were expected to fill the remaining octahedral voids.

The crystal structure of the sample was examined by means of powder X-ray diffraction (pXRD) using a Bruker D2 Phaser diffractometer equipped with a solid-state LynxEye XE-T detector and a Cu Kα X-ray source. XRD patterns were processed by means of the Rietveld refinement method using the Fullprof software package.[20]

Heat capacity and electrical resistivity measurements were performed using a Quantum Design Physical Property Measurement System (PPMS). The standard two τ time-relaxation method was used to measure the heat capacity. For electrical transport measurements, four thin platinum wire leads were attached to the sample surface using an Epo-Tek H20E conductive silver epoxy. Measurements were carried out in the temperature range of T = 1.9−300 K.

Electronic structure calculations were performed by means of density functional theory (DFT) using the Quantum Espresso (QE) version 6.7 package[21−23] using the Perdew−Burke−Ernzerhof (PBE) generalized gradient approximation (GGA)[25] of the exchange−correlation (*xc*) potential. Scalar relativistic and fully relativistic projector-augmented wave (PAW)[24,25] sets were taken from the PSlib database.[26] A QE input file was produced using the generator tool available in the Materials Cloud platform.[27] The experimental unit cell parameter was relaxed using the Broyden−Fletcher−Goldfarb−Shanno (BFGS) algorithm and a 9 × 9 × 9 k-point mesh. The kinetic energy cutoff for charge density and wave functions was set to 58 Ry and 522 Ry, respectively. Density of states integrations within the irreducible wedge of the primitive Brillouin zone were completed on an 18 × 18 × 18 k-point mesh. Electron transfer was assessed using the Bader charge analysis method.[28−30] For the accurate analysis of the charge, the charge density cutoff was increased to 1200 Ry in a SCF run to yield a denser Fourier-transformed charge density grid. Visualization of the covalent bonding within the crystal structure was done by plotting the Density Overlap Regions Indicator (DORI) introduced by de Silva and Corminboeuf.[31] Charge density critical points were analyzed using the CRITIC2 code.[32]

The calculation of the electronic structure of the disordered $MgPd_{1.25}Sb$ compound was performed by means of the Korringa−Kohn−Rostoker (KKR) multiple scattering DFT method employing the coherent potential approximation (CPA) to model the Pd site disorder, as implemented in the SPR KKR package.[33] The PBE GGA *xc* potential was used, and the calculations were performed in a fully relativistic, spin-polarized mode. The structure was modeled with an $Fm\bar{3}m$ unit cell. The lattice parameter of MgPdSb relaxed using QE was expanded by 0.8% for $MgPd_{1.25}Sb$, in agreement with pXRD results. To model the effect of possible minute amount of Pd interstitials in the parent MgPdSb compound, the KKR calculations were also performed on a $MgPdPd_{0.04}Sb$ phase in which 4% of 4*d* sites is occupied by Pd.

RESULTS AND DISCUSSION

Analysis of the pXRD pattern (Figure 2) showed that a single-phase sample of MgPdSb with a lattice parameter a = 6.2841(1) Å was obtained after the second annealing step. Rietveld refinement confirmed the assumed $F\bar{4}3m$ cubic half-Heusler structure. In the case of the $MgPd_{1+x}Sb$ series, only the sample with the lowest Pd content (x = 0.25) was found to be single phase. Samples with higher Pd concentration contained a PdSb impurity (see Figure S3 of the Supporting Material).

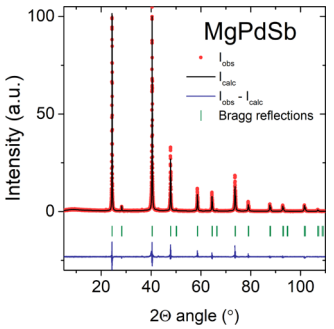

Figure 2. Powder XRD pattern of MgPdSb (red points) with a Rietveld fit (black line). The blue line shows a difference between the observed and model intensity. Green ticks mark the expected positions of Bragg reflections for the half-Heusler ($F\bar{4}3m$) phase.

Rietveld analysis shows no sign of significant interstitial concentration on the nominally vacant 4*d* site, as presented in a difference Fourier electron density map (see Figure 3;

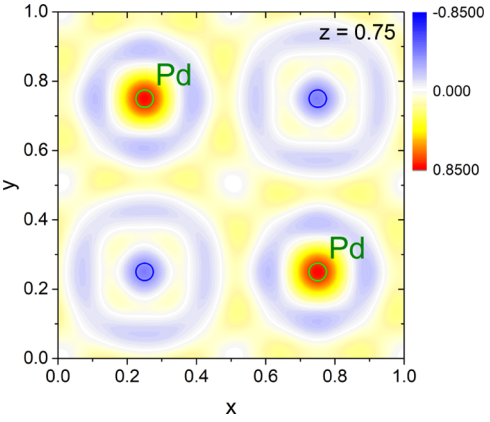

Figure 3. Difference Fourier electron density map calculated for MgPdSb from the powder XRD data (F_{obs}) and the Rietveld-refined model (F_{calc}). No significant concentration of interstitial atoms is observed in the unfilled octahedral voids (marked with blue circles) in the unit cell. Green circles mark the positions of Pd atoms at the 4*c* site.

https://doi.org/10.1021/acs.jpcc.2c01367
J. Phys. Chem. C 2022, 126, 14229−14235

observed electron density is shown in Figure S4a). The refinement of Pd occupancy at the 4*d* site leads to at most 4%. Such a small occupancy does not affect the electronic structure of MgPdSb around the Fermi level (see Figure S5 of the Supporting Material).

Rietveld refinement on the pXRD pattern of $MgPd_{1.25}Sb$ (Figure S6 of the Supporting Material) suggests that all additional Pd atoms occupy the vacant 4*d* octahedral voids, while the MgPdSb half-Heusler structure remains intact. This has an important implication for the electronic structure as will be shown in the following paragraphs. If, instead, Pd is assumed to be randomly distributed over all of the octahedral voids (resulting in a centrosymmetric defective full-Heusler structure), the refinement yields an unphysically high isotropic thermal displacement factor for Mg (B_{iso} > 11 Å^2, see Table S2 of the Supporting Material).

Results of electronic structure calculations for stoichiometric MgPdSb are presented in Figure 4. The band structure shows a

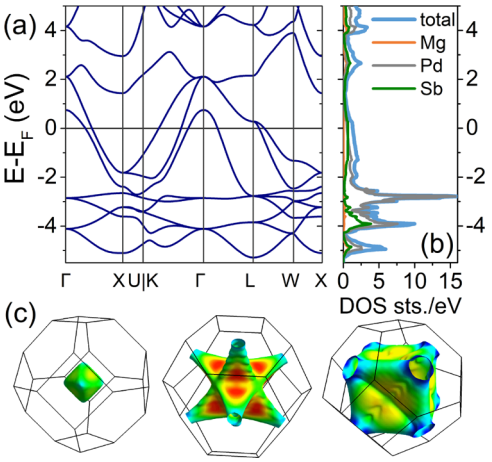

Figure 4. Band structure of MgPdSb (a) along with the atom-projected DOS (b). Three distinct bands cross the E_F as is easily seen along the Γ−K line, resulting in a Fermi surface (FS) consisting of three parts, as plotted in panel (c). FS is colored according to the Fermi velocity from blue to red.

metallic character. Three distinct bands cross the Fermi level (Figure 4a), resulting in a Fermi surface (FS) depicted in Figure 4c. The overall shape of the FS is similar to the one found in full-Heusler compounds, such as $LiGa_2Ir$,[34] $LiPd_2Ge$,[35] and $MgPd_2Sb$.[19] The electronic DOS around the Fermi level is mostly contributed by Pd *d* and Sb *p* states (Figure 4b).

Bader charge analysis yields a charge of +1.53 *e* at the Mg atom, in agreement with the low electronegativity of Mg compared to those of Pd and Sb. Pd and Sb attain a negative Bader charge of −1.34 *e* and −0.19 *e*, respectively. A strong electron transfer from Mg to Pd and rather weak to Sb might seem counterintuitive based on the common electronegativity scales, where Pd is either less electronegative (as in Allred−Rochow[36] and Allen[37] scales as well as in the recent definition of electronegativity by Rahm et al.[38]) or only slightly more electronegative than Sb (Pauling scale: χ_{Pd} = 2.2, χ_{Sb} = 2.1). This electron transfer picture is, however, consistent with the picture of the half-Heusler phase as an "electronically active" ZnS-type $(PdSb)^{2-}$ sublattice intertwined with a Mg^{2+} donor network. The presence of Pd−Sb covalent bonding is visible in the calculated electron density (Figure S7 of the Supporting Material). A bond critical point (saddle point of electron density) is found between Pd and Sb (Figure S8), and the DORI[31] analysis (Figure S9) shows a covalent Pd−Sb bond.

As was discussed by Zeier et al.,[5] the half-Heusler phases usually form with compositions corresponding to VEC = 18. This was rationalized by a molecular orbital picture taking as an example the semiconducting ZrNiSn phase (VEC = 4 + 10 + 4 = 18): with 18 valence electrons, the t_2 orbital, resulting from the interaction between Ni and Zr d_{xy}, d_{xz}, and d_{yz} atomic orbitals, is completely filled (Figure 5a).

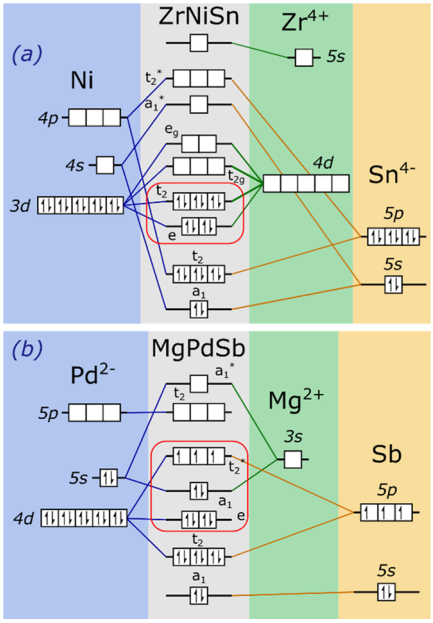

Figure 5. Schematic MO diagram for ZrNiSn (modified from Zeier *et al.*[5]) (a) and MgPdSb (b). Orbital energies are not shown to scale.

In the case of MgPdSb, the order of crystal orbitals is different (Figure 5b). Since for Mg the frontier orbital is 3*s*, the interactions between Mg and PdSb sublattice are qualitatively distinct from those of Zr with NiSn, where Zr 4*d* states overlap with t_2 and e MOs of NiSn. This yields an a_1 orbital between the e doublet and t_2 triplet. With 17 valence electrons, the t_2 orbital (antibonding Pd *d*−Sb *p* interaction) is half filled, consistent with a finite DOS(E_F) contributed by Pd and Sb (see Figure 4b). In this case, VEC = 18 does not correspond to a closed-shell configuration, which would be attained for VEC = 20. However, since the partially filled t_2 shell is (weakly) antibonding, such a high VEC would likely destabilize the half-Heusler structure.

A hypothetical example of a compound with VEC = 20 with Mg would be a ZnS-type CdTe with Mg atoms occupying the interstitial positions of the zinc blende sublattice. This would, however, require that either Mg or Cd be electroneutral. Such a counterintuitive electronic configuration shows that the Mg- and Li-based half-Heusler phases are definitively metallic and cannot be driven semiconducting by increasing the electron count.

Inspection of the Materials Project database shows that Mg-bearing half-Heusler phases with VEC = 18 (e.g., MgAgAs and MgCuSb, see Figure 6a,b) indeed show a finite DOS(E_F). At the same time, phases with VEC = 17 having an early transition metal at the A site show a gap slightly above the E_F, suggesting

https://doi.org/10.1021/acs.jpcc.2c01367
J. Phys. Chem. C 2022, 126, 14229−14235

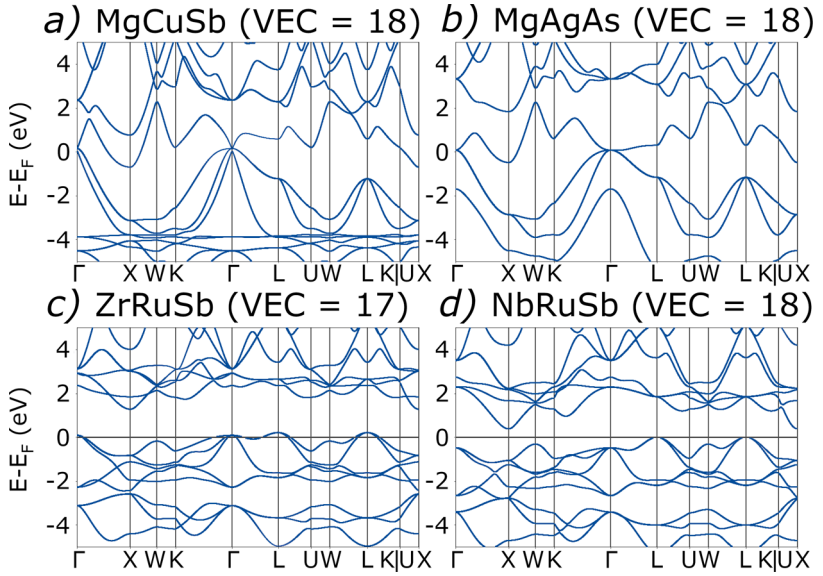

Figure 6. Band structures of MgCuSb and MgAgAs (panels (a) and (b); VEC = 18), ZrRuSb (panel (c); VEC = 17), and NbRuSb (panel (d); VEC = 18) taken from the Materials Project database[41] (database IDs: *mp-3522*, *mp-3477*, *mp-31457*, *mp-505297*, respectively) using the pymatgen library.[42] For ZrRuSb and NbRuSb, the Fermi level is indicated as a horizontal line to highlight that the former, electron-poor compound is a metal, while the latter is a semiconductor.

that increasing the electron count to VEC = 18 would make them semiconducting (see Figure 6c,d).

There are 43 Li-based half-Heusler compounds, 42 of which have VEC = 8 or 18 (LiAuSb is the only reported compound with VEC = 17, see Table S1 of the Supporting Material). Due to the same symmetry of the frontier orbital (2*s* in Li, 3*s* in Mg), the electronic structure of LiAuSb (shown in Figure S10 of the Supporting Material) is qualitatively similar to that of MgPdSb (Figure 4a). This similarity can be considered an example of the so-called diagonal relationship (or isodiagonality) of Li and Mg, which is found in many different aspects of chemistry of the two elements (as well as other element pairs).[39,40]

Results of KKR CPA calculations are shown in Figure 7. The density of states for the Pd-stuffed compound strongly depends on the way the Pd is distributed over the eight octahedral voids of the MgSb sublattice. If one assumes that all Pd atoms are randomly distributed over all of the voids, the band structure (in the case of a disordered solid represented by the Bloch spectral function—BSF) is slightly shifted with respect to the Fermi level to accommodate for additional electrons (Figure 7e,f). The overall shape remains only weakly affected, but the Pd *d* band becomes smeared and broadened. If, however, we assume that the MgPdSb lattice remains intact and the additional Pd atoms occupy the vacant voids (consistent with pXRD analysis), the additional Pd *d* states form strongly localized, nondispersive bands at 6−7 eV below E_F and the remaining bands are only slightly affected (Figure 7c,d). The latter model is in line with the discussion of electroneutral Ni^0 interstitials in the $ZrNi_{1+x}Si$ phase by Zeier *et al.*[5]

The results of KKR CPA calculations are consistent with the measurements of low-temperature heat capacity of MgPdSb and $MgPd_{1.25}Sb$ (Figure 8), which were fitted with the equation $C_p/T(T^2) = \gamma + \beta_3 T^2 + \beta_5 T^4$. Both phases show a very similar value of the electronic (Sommerfeld) heat capacity coefficient $\gamma = 3.3(1)$ mJ mol^{-1} K^{-2} for pristine MgPdSb and $\gamma = 3.5(2)$ mJ mol^{-1} K^{-2} for the Pd-stuffed variant. As shown in Figure 7a−d, the band structure/BSF and DOS at the Fermi

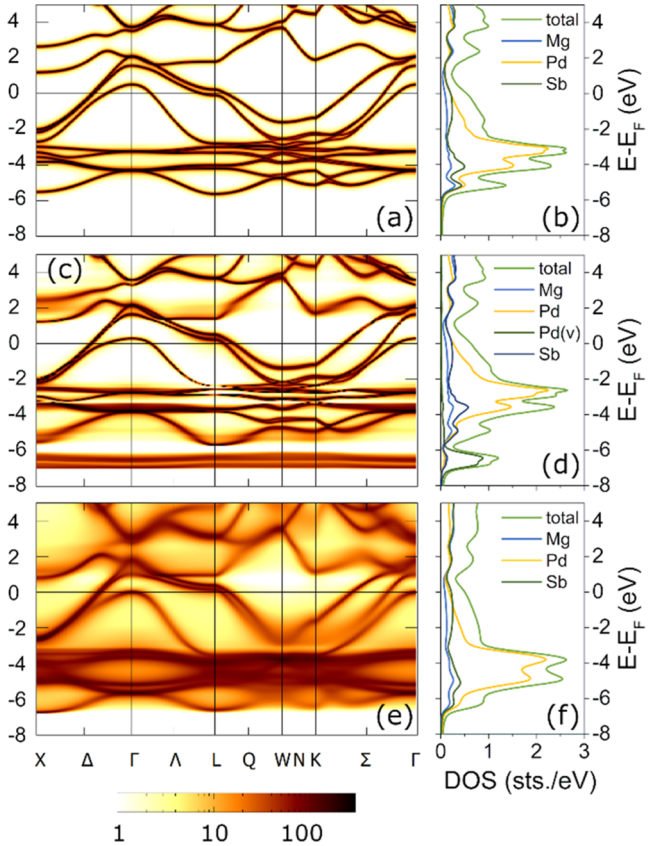

Figure 7. Bloch spectral functions (a, c, e) and DOS (b, d, f) calculated for a pristine MgPdSb (a, b), "$MgPdPd_{0.25}Sb$"—the half-Heusler (NCS) cell with additional Pd atoms randomly distributed over the four octahedral voids (c, d), and "$MgPd_{1.25}Sb$"—the full-Heusler (centrosymmetric) cell with eight octahedral voids randomly occupied by Pd with a 62.5% probability.

level are almost unaffected by the introduction of additional Pd atoms. Since the γ coefficient is linearly proportional to the

https://doi.org/10.1021/acs.jpcc.2c01367
J. Phys. Chem. C 2022, 126, 14229−14235

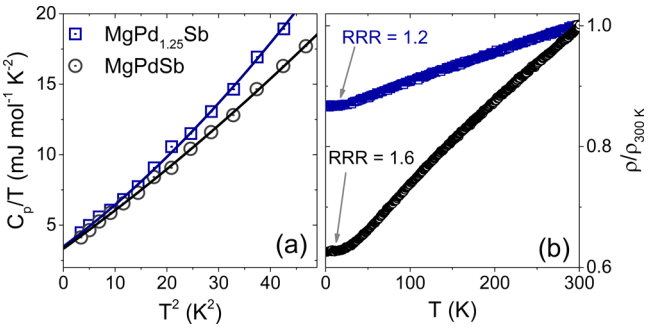

Figure 8. Panel (a) shows the low-temperature heat capacity of MgPdSb and $MgPd_{1.25}Sb$ (black and blue points) along with a fit to the equation $C_p/T(T^2) = \gamma + \beta_3 T^2 + \beta_5 T^4$ (solid lines). Panel (b) shows the resistivity of both materials normalized to the room temperature resistivity ($\rho_{300\,K}$). The Pd-stuffed sample shows a higher residual resistivity and thus a much lower residual resistivity ratio RRR = $\rho_{300\,K}/\rho_0$.

electronic density of states (which itself is renormalized by interactions, including electron−phonon coupling, as described in the following paragraph), the almost unchanged value of γ and DOS(E_F) suggests that the electron−phonon coupling is not strongly affected by additional Pd atoms. Phonon coefficients for the MgPdSb phase (β_3 = 0.26(2) mJ mol^{-1} K^{-4} and β_5 = 1.0(4) μJ mol^{-1} K^{-6}) are similar for the $MgPd_{1.25}Sb$ phase (β_3 = 0.27(2) mJ mol^{-1} K^{-4} and β_5 = 2.2(5) μJ mol^{-1} K^{-6}). The corresponding values of the Debye temperatures calculated from β_3 are Θ_D = 282(7) K and Θ_D = 287(7) K for MgPdSb and $MgPd_{1.25}Sb$, respectively.

The electron−phonon coupling coefficient was estimated for the stoichiometric MgPdSb by comparing the calculated and experimental value of the Sommerfeld coefficient γ

$$\lambda_{ep} = \frac{\gamma_{expt}}{\gamma_{calc}} - 1$$

This yields $\lambda_{ep} \approx 0.03$, suggesting very weak coupling between conduction electrons and lattice vibrations. This is consistent with no superconducting transition observed down to T = 1.85 K.

It is worth noting that the synthesized polycrystalline pellet of MgPdSb has a distinct purple hue. While intermetallics are generally plain silver, a number of compounds with *fcc*-derived crystal structures are reported to show some distinct color.[43] This stems from their distinctive band structures with narrow *d* bands lying ca. 1.7−3.0 eV below the Fermi level. A number of Heusler and half-Heusler compounds are reported to show a distinctive color.[43,44] In MgPdSb, the narrow Pd *d* band is situated ca. 2.5−2.9 eV below the E_F (Figure 4a), corresponding to an excitation wavelength of ca. 480−500 nm. The light reflected from the sample is then depleted of the green-blue part of the spectrum and appears purplish.

The temperature-dependent resistivity of MgPdSb (Figure 8b) shows a behavior typical for metals. This is in agreement with the aforementioned results of DFT computations. No sign of superconducting transition is observed down to T = 1.9 K. The Pd-stuffed $MgPd_{1.25}Sb$ shows a higher residual resistivity (RRR = 1.2 vs RRR = 1.6 for MgPdSb), consistent with the presence of atomic disorder.

CONCLUSIONS

We have successfully synthesized an electron-deficient half-Heusler phase MgPdSb along with its Pd-stuffed modification $MgPd_{1.25}Sb$ and discussed their electronic structure based on DFT calculations and molecular orbital theory. The introduction of additional Pd atoms does not strongly affect the electronic structure as evidenced by both electronic structure calculations and heat capacity measurements.

We have shown that Mg-based half-Heusler compounds show a qualitatively different electronic structure compared to the more prevalent phases hosting an early transition metal or lanthanide. The difference stems from the symmetry of the frontier orbital of Mg. Thus, in contrary to TM- and lanthanide-based analogues, Mg-based (and by analogy Li-based) half-Heusler phases remain metallic even at the "perfect" valence electron count (VEC) of 18 and cannot be driven semiconducting by altering the electron count alone.

ASSOCIATED CONTENT

Supporting Information

The Supporting Information is available free of charge at https://pubs.acs.org/doi/10.1021/acs.jpcc.2c01367.

Details of the synthesis method, tables of reported half-Heusler compounds, XRD patterns of $MgPd_{1+x}Sb$ samples (x = 0.25, 0.50, 0.75), Fourier electron density maps for MgPdSb, results of Rietveld refinement for MgPdSb and $MgPd_{1.25}Sb$, band structure of LiAuSb, and calculated electron density together with chemical bonding indicators of MgPdSb (PDF)

AUTHOR INFORMATION

Corresponding Author

Tomasz Klimczuk − *Faculty of Applied Physics and Mathematics and Advanced Materials Center, Gdansk University of Technology, 80-232 Gdansk, Poland;* orcid.org/0000-0002-7089-4631; Email: michal.winiarski@pg.edu.pl

Authors

Michał J. Winiarski − *Faculty of Applied Physics and Mathematics and Advanced Materials Center, Gdansk University of Technology, 80-232 Gdansk, Poland;* orcid.org/0000-0001-9083-8066

Kamila Stolecka − *Faculty of Applied Physics and Mathematics and Advanced Materials Center, Gdansk University of Technology, 80-232 Gdansk, Poland*

Leszek Litzbarski − *Faculty of Applied Physics and Mathematics and Advanced Materials Center and Department of Mechatronics and High Voltage Engineering, Faculty of Electrical and Control Engineering, Gdansk University of Technology, 80-232 Gdansk, Poland*

Thao T. Tran − *Department of Chemistry, Clemson University, Clemson, South Carolina 29634, United States;* orcid.org/0000-0002-2395-3555

Karolina Górnicka − *Faculty of Applied Physics and Mathematics and Advanced Materials Center, Gdansk University of Technology, 80-232 Gdansk, Poland*

Complete contact information is available at: https://pubs.acs.org/10.1021/acs.jpcc.2c01367

Author Contributions

The manuscript was written through contributions of all authors.

Notes

The authors declare no competing financial interest.

■ ACKNOWLEDGMENTS

The research at Gdansk University of Technology was supported by the National Science Centre (Poland) grant (UMO-2017/27/B/ST5/03044). T.T.T. thanks Clemson University, College of Science, and Department of Chemistry for support.

■ ABBREVIATIONS

BSF, Bloch spectral function; CPA, coherent potential approximation; DOS, density of (electronic) states; KKR, Korringa−Kohn−Rostoker; MO, molecular orbital; NCS, noncentrosymmetric; pXRD, powder X-ray diffraction; RRR, residual resistivity ratio; TM, transition metal; VEC, valence electron count

■ REFERENCES

(1) Gzyl, A. S.; Oliynyk, A. O.; Mar, A. Half-Heusler Structures with Full-Heusler Counterparts: Machine-Learning Predictions and Experimental Validation. *Cryst. Growth Des.* **2020**, *20*, 6469−6477.
(2) Gzyl, A. S.; Mar, A.; Oliynyk, A. O. Machine Learning in Solid-State Chemistry: Heusler Compounds. In *Encyclopedia of Inorganic and Bioinorganic Chemistry*; John Wiley & Sons, Ltd., 2021; pp 1−15.
(3) Tolborg, K.; Iversen, B. B. Chemical Bonding Origin of the Thermoelectric Power Factor in Half-Heusler Semiconductors. *Chem. Mater.* **2021**, *33*, 5308−5316.
(4) Fu, C.; Bai, S.; Liu, Y.; Tang, Y.; Chen, L.; Zhao, X.; Zhu, T. Realizing High Figure of Merit in Heavy-Band p -Type Half-Heusler Thermoelectric Materials. *Nat. Commun.* **2015**, *6*, No. 8144.
(5) Zeier, W. G.; Schmitt, J.; Hautier, G.; Aydemir, U.; Gibbs, Z. M.; Felser, C.; Snyder, G. J. Engineering Half-Heusler Thermoelectric Materials Using Zintl Chemistry. *Nat. Rev. Mater.* **2016**, *1*, 1−10.
(6) Zhu, T.; Fu, C.; Xie, H.; Liu, Y.; Zhao, X. High Efficiency Half-Heusler Thermoelectric Materials for Energy Harvesting. *Adv. Energy Mater.* **2015**, *5*, No. 1500588.
(7) Al-Sawai, W.; Lin, H.; Markiewicz, R. S.; Wray, L. A.; Xia, Y.; Xu, S.-Y.; Hasan, M. Z.; Bansil, A. Topological Electronic Structure in Half-Heusler Topological Insulators. *Phys. Rev. B* **2010**, *82*, No. 125208.
(8) Lin, H.; Wray, L. A.; Xia, Y.; Xu, S.; Jia, S.; Cava, R. J.; Bansil, A.; Hasan, M. Z. Half-Heusler Ternary Compounds as New Multifunctional Experimental Platforms for Topological Quantum Phenomena. *Nat. Mater.* **2010**, *9*, 546−549.
(9) Tafti, F. F.; Fujii, T.; Juneau-Fecteau, A.; René de Cotret, S.; Doiron-Leyraud, N.; Asamitsu, A.; Taillefer, L. Superconductivity in the Noncentrosymmetric Half-Heusler Compound LuPtBi: A Candidate for Topological Superconductivity. *Phys. Rev. B* **2013**, *87*, No. 184504.
(10) Pavlosiuk, O.; Kaczorowski, D.; Wiśniewski, P. Shubnikov - de Haas Oscillations, Weak Antilocalization Effect and Large Linear Magnetoresistance in the Putative Topological Superconductor LuPdBi. *Sci. Rep.* **2015**, *5*, No. 9158.
(11) Pavlosiuk, O.; Kaczorowski, D.; Wiśniewski, P. Superconductivity and Shubnikov–de Haas Oscillations in the Noncentrosymmetric Half-Heusler Compound YPtBi. *Phys. Rev. B* **2016**, *94*, No. 035130.
(12) Pavlosiuk, O.; Kaczorowski, D.; Fabreges, X.; Gukasov, A.; Wiśniewski, P. Antiferromagnetism and Superconductivity in the Half-Heusler Semimetal HoPdBi. *Sci. Rep.* **2016**, *6*, No. 18797.
(13) Dshemuchadse, J.; Steurer, W. More Statistics on Intermetallic Compounds − Ternary Phases. *Acta Crystallogr., Sect. A: Found. Adv.* **2015**, *71*, 335−345.
(14) Anand, S.; Xia, K.; Hegde, V. I.; Aydemir, U.; Kocevski, V.; Zhu, T.; Wolverton, C.; Jeffrey Snyder, G. A Valence Balanced Rule for Discovery of 18-Electron Half-Heuslers with Defects. *Energy Environ. Sci.* **2018**, *11*, 1480−1488.
(15) Zeier, W. G.; Anand, S.; Huang, L.; He, R.; Zhang, H.; Ren, Z.; Wolverton, C.; Snyder, G. J. Using the 18-Electron Rule To Understand the Nominal 19-Electron Half-Heusler NbCoSb with Nb Vacancies. *Chem. Mater.* **2017**, *29*, 1210−1217.
(16) Roth, N.; Zhu, T.; Iversen, B. B. A Simple Model for Vacancy Order and Disorder in Defective Half-Heusler Systems. *IUCrJ* **2020**, *7*, 673−680.
(17) Anand, S.; Wood, M.; Xia, Y.; Wolverton, C.; Snyder, G. J. Double Half-Heuslers. *Joule* **2019**, *3*, 1226−1238.
(18) Drews, J.; Eberz, U.; Schuster, H.-U. Optische Untersuchungen an farbigen Intermetallischen phasen. *J. Less-Common Met.* **1986**, *116*, 271−278.
(19) Winiarski, M. J.; Kuderowicz, G.; Górnicka, K.; Litzbarski, L. S.; Stolecka, K.; Wiendlocha, B.; Cava, R. J.; Klimczuk, T. $MgPd_2Sb$: A Mg-Based Heusler-Type Superconductor. *Phys. Rev. B* **2021**, *103*, No. 214501.
(20) Rodríguez-Carvajal, J. Recent Advances in Magnetic Structure Determination by Neutron Powder Diffraction. *Phys. B: Condens. Matter* **1993**, *192*, 55−69.
(21) Giannozzi, P.; Baroni, S.; Bonini, N.; Calandra, M.; Car, R.; Cavazzoni, C.; Ceresoli, D.; Chiarotti, G. L.; Cococcioni, M.; Dabo, I.; et al. QUANTUM ESPRESSO: A Modular and Open-Source Software Project for Quantum Simulations of Materials. *J. Phys.: Condens. Matter* **2009**, *21*, No. 395502.
(22) Giannozzi, P.; Andreussi, O.; Brumme, T.; Bunau, O.; Nardelli, M. B.; Calandra, M.; Car, R.; Cavazzoni, C.; Ceresoli, D.; Cococcioni, M.; et al. Advanced Capabilities for Materials Modelling with Quantum ESPRESSO. *J. Phys.: Condens. Matter* **2017**, *29*, No. 465901.
(23) Giannozzi, P.; Baseggio, O.; Bonfà, P.; Brunato, D.; Car, R.; Carnimeo, I.; Cavazzoni, C.; de Gironcoli, S.; Delugas, P.; Ferrari Ruffino, F.; et al. Quantum ESPRESSO toward the Exascale. *J. Chem. Phys.* **2020**, *152*, No. 154105.
(24) Blöchl, P. E. Projector Augmented-Wave Method. *Phys. Rev. B* **1994**, *50*, 17953−17979.
(25) Kresse, G.; Joubert, D. From Ultrasoft Pseudopotentials to the Projector Augmented-Wave Method. *Phys. Rev. B* **1999**, *59*, 1758−1775.
(26) Dal Corso, A. Pseudopotentials Periodic Table: From H to Pu. *Comput. Mater. Sci.* **2014**, *95*, 337−350.
(27) Talirz, L.; Kumbhar, S.; Passaro, E.; Yakutovich, A. V.; Granata, V.; Gargiulo, F.; Borelli, M.; Uhrin, M.; Huber, S. P.; Zoupanos, S.; et al. Materials Cloud, a Platform for Open Computational Science. *Sci. Data* **2020**, *7*, No. 299.
(28) Henkelman, G.; Arnaldsson, A.; Jónsson, H. A Fast and Robust Algorithm for Bader Decomposition of Charge Density. *Comput. Mater. Sci.* **2006**, *36*, 354−360.
(29) Tang, W.; Sanville, E.; Henkelman, G. A Grid-Based Bader Analysis Algorithm without Lattice Bias. *J. Phys.: Condens. Matter* **2009**, *21*, No. 084204.
(30) Sanville, E.; Kenny, S. D.; Smith, R.; Henkelman, G. Improved grid-based algorithm for Bader charge allocation. *J. Comput. Chem.* **2007**, *28*, 899−908.
(31) de Silva, P.; Corminboeuf, C. Simultaneous Visualization of Covalent and Noncovalent Interactions Using Regions of Density Overlap. *J. Chem. Theory Comput.* **2014**, *10*, 3745−3756.
(32) Otero-de-la-Roza, A.; Johnson, E. R.; Luaña, V. Critic2: A Program for Real-Space Analysis of Quantum Chemical Interactions in Solids. *Comput. Phys. Commun.* **2014**, *185*, 1007−1018.
(33) Ebert, H.; Ködderitzsch, D.; Minár, J. Calculating Condensed Matter Properties Using the KKR-Green's Function Method-Recent

https://doi.org/10.1021/acs.jpcc.2c01367
J. Phys. Chem. C 2022, 126, 14229−14235

Developments and Applications. *Rep. Prog. Phys.* **2011**, *74*, No. 096501.
(34) Górnicka, K.; Kuderowicz, G.; Winiarski, M. J.; Wiendlocha, B.; Klimczuk, T. Superconductivity in LiGa2Ir Heusler Type Compound with VEC = 16. *Sci. Rep.* **2021**, *11*, No. 16517.
(35) Górnicka, K.; Kuderowicz, G.; Carnicom, E. M.; Kutorasiński, K.; Wiendlocha, B.; Cava, R. J.; Klimczuk, T. Soft-Mode Enhanced Type-I Superconductivity in $LiPd_2Ge$. *Phys. Rev. B* **2020**, *102*, No. 024507.
(36) Allred, A. L.; Rochow, E. G. A Scale of Electronegativity Based on Electrostatic Force. *J. Inorg. Nucl. Chem.* **1958**, *5*, 264−268.
(37) Allen, L. C. Electronegativity Is the Average One-Electron Energy of the Valence-Shell Electrons in Ground-State Free Atoms. *J. Am. Chem. Soc.* **1989**, *111*, 9003−9014.
(38) Rahm, M.; Zeng, T.; Hoffmann, R. Electronegativity Seen as the Ground-State Average Valence Electron Binding Energy. *J. Am. Chem. Soc.* **2019**, *141*, 342−351.
(39) Rayner-Canham, G. Periodic Patterns. *J. Chem. Educ.* **2000**, *77*, 1053.
(40) Rayner-Canham, G. Isodiagonality in the Periodic Table. *Found. Chem.* **2011**, *13*, 121−129.
(41) Jain, A.; Ong, S. P.; Hautier, G.; Chen, W.; Richards, W. D.; Dacek, S.; Cholia, S.; Gunter, D.; Skinner, D.; Ceder, G.; Persson, K. A. Commentary: The Materials Project: A Materials Genome Approach to Accelerating Materials Innovation. *APL Mater.* **2013**, *1*, No. 011002.
(42) Ong, S. P.; Richards, W. D.; Jain, A.; Hautier, G.; Kocher, M.; Cholia, S.; Gunter, D.; Chevrier, V. L.; Persson, K. A.; Ceder, G. Python Materials Genomics (Pymatgen): A Robust, Open-Source Python Library for Materials Analysis. *Comput. Mater. Sci.* **2013**, *68*, 314−319.
(43) Pöttgen, R.; Johrendt, D. *Intermetallics, Synthesis, Structure, Function*, 2nd ed.; De Gruyter: Berlin, Boston, 2019.
(44) Mishra, V.; Iyer, A. K.; Mumbaraddi, D.; Oliynyk, A. O.; Zuber, G.; Boucheron, A.; Dmytriv, G.; Bernard, G. M.; Michaelis, V. K.; Mar, A. Coloured Intermetallic Compounds $LiCu_2Al$ and $LiCu_2Ga$. *J. Solid State Chem.* **2020**, *292*, No. 121703.

https://doi.org/10.1021/acs.jpcc.2c01367
J. Phys. Chem. C 2022, 126, 14229−14235